

1 Crystal plane dependent dispersion of cobalt metal on metastable 2 aluminas

3 Ilya V. Yakovlev,^{a, b, c} Vladimir I. Zaikovskii,^b Mariya A. Kazakova,^b Evgeniy S. Papulovskiy,^b
4 Olga B. Lapina,^{a, b} and Jean-Baptiste d'Espinose de Lacaillerie^{c, *}

5 ^a Novosibirsk State University, Pirogova Street 1, 630090 Novosibirsk, Russia

6 ^b Boreskov Institute of Catalysis SB RAS, Prospekt Lavrentieva 5, 630090, Novosibirsk, Russia

7 ^c SIMM, UMR CNRS 7615, ESPCI Paris, Université PSL, Sorbonne Université, 10 Rue
8 Vauquelin, 75005 Paris, France

9 * Corresponding author. Email address: jean-baptiste.despinose@espci.fr

10 **Abstract**

11

12 Metallic Co nanoparticles, widely used and studied as supported heterogeneous catalysts for
13 Fischer-Tropsch synthesis (FTS), display catalytic properties that can vary significantly depending
14 on their size and crystal structure. In this work, we used ⁵⁹Co Internal Field NMR (⁵⁹Co IF NMR)
15 complemented by high-resolution transmission electron microscopy (HRTEM) to demonstrate the
16 influence of strong metal-support interaction on two noticeably different metastable alumina
17 phases - γ -Al₂O₃ and χ -Al₂O₃. According to ⁵⁹Co IF NMR and HRTEM, the metallic particles
18 supported on χ -Al₂O₃ were larger and displayed a significantly higher content of *hcp* Co phase,
19 which are known to be more active and selective to C₅₊ in FTS. The ¹H NMR chemical shifts of
20 hydroxyl groups anchored to the (110) and (111) spinel crystal planes were calculated by DFT. It
21 revealed that the hydroxyl coverage of γ -Al₂O₃ facilitates the dispersion of Co precursor over the
22 surface of the support, ultimately leading to the formation of smaller metal Co nanoparticles on γ -
23 Al₂O₃, than on χ -Al₂O₃.

24

25 **Keywords:** heterogeneous catalysis, ⁵⁹Co NMR, HRTEM, Internal Field NMR, DFT, metal
26 support interaction, Fischer-Tropsch synthesis

1 Introduction

The catalytic properties of nanoparticles (NPs) strongly depend on their size, crystal structure and morphology – factors that have a complex interconnection with each other but that are, to some extent, controllable by adjusting the synthesis conditions. An important case study is metallic cobalt supported on oxides whose catalytic behavior depends strongly on the metal-support interaction in ways that are not yet fully understood.[1] In Fischer-Tropsch synthesis (FTS) for example, the choice of the support as well as possible decorations with various noble metal promoters are used to control the morphology and crystal structure of cobalt NPs in order to obtain the desired catalytic properties. The influence of these two properties of Co NPs on activity and selectivity towards C_{5+} hydrocarbons has been extensively studied in the recent decades resulting in some generally agreed-upon requirements. First, vast experimental data [2–7] indicate that, between the two most common structures met in metallic cobalt, the hexagonal close-packed (*hcp*) crystal structure is more active and selective towards C_{5+} than the face-centered cubic (*fcc*) one. Second, experimental data and theoretical calculations show that below a certain size (between 4 and 10 nm according to different sources) Co NPs become much less active in FTS and their selectivity shifts to CH_4 [8–13]. However, in many instances, how the desired cobalt size and structure are tailored by the support remains an open question.

During the preparation step, how the support directs the speciation of Co(II) ions and complexes from the precursor has been efficiently investigated by spectroscopic means (noticeably UV-visible spectroscopy[14] and EXAFS[15]), rationalized through coordination chemistry[16] and modeled by DFT.[17] Nevertheless, the interaction with the support of the larger Co nanoparticles obtained after reduction is paradoxically more difficult to characterize or model.[18]

Co nanoparticles can be characterized by a variety of physical methods: X-Ray diffraction (XRD), electron microscopy techniques (transmission, scanning, or scanning transmission), magnetometry, magnetic resonance techniques (electronic ferromagnetic resonance - FMR, ^{59}Co Internal Field nuclear magnetic resonance – IF NMR). All of these techniques have their own experimental limitations and provide different kinds of structural information. In this work, we rely on a combination of ^{59}Co Internal Field NMR (^{59}Co IF NMR) and high-resolution transmission electron microscopy (HRTEM), a combination that proved effective in some of our previous works.[19–22] HRTEM is an indispensable technique providing unique information on the morphology of the particles close to the single-atom scale. However, the intrinsic limitation of this technique is its local character, making it necessary to extrapolate the data obtained from a limited set of micrographs. ^{59}Co IF NMR, on the contrary, is a bulk technique that was shown to provide information on the crystal and magnetic structures of Co nanoparticles [19,20,23–26] as

61 well as on their size distribution,[21,27] even though it is limited by the intrinsically low intensity
62 of the NMR signal and the difficulty of spectral analysis.

63 We focus here on the role of two low-temperature metastable alumina phases, γ -Al₂O₃ and
64 χ -Al₂O₃, in directing the dispersion and structure of Co nanoparticles. γ -Al₂O₃ is a well-studied
65 and widely employed support in Co FTS catalysts. It has a high specific surface area and
66 demonstrates good stability under usual reaction conditions when stabilized by metal oxides. χ -
67 Al₂O₃ is the lowest temperature form of alumina in the gibbsite alumina series; the use of this
68 metastable phase as a catalyst support has been investigated to a much lesser extent, even though
69 it also demonstrates a relatively high specific surface area and thermal stability. Pansanga et al.
70 have demonstrated that the use of a mixed χ -Al₂O₃ + γ -Al₂O₃ support leads to increased Co
71 dispersion at high Co loadings, but this effect could be mostly due to the morphology of the
72 particles and not necessarily to their surfaces structures [28]. The crystal structure as well as
73 crystallite stacking of χ -Al₂O₃ still remain an open question with several equally feasible viewpoint
74 (see for instance a recent mini-review by Prins [29]). Nevertheless, regardless of the preferred
75 theory on the structure of bulk γ -Al₂O₃ and χ -Al₂O₃, an important difference between these
76 alumina phases lies in the different crystal faces that dominate the surface of the particles.[30,31]
77 As a result, χ -Al₂O₃ differs from γ -Al₂O₃ by the type and density of defect surface sites [32] and
78 by having a higher surface density of weak Lewis acid sites.[33,34] These differences have been
79 suggested to explain different metal sintering behavior.[35] Regarding specifically Co, the
80 presence of χ -phase in γ -Al₂O₃ resulted in higher dispersion of Co as well as higher CO
81 hydrogenation activities of the Co/Al₂O₃ catalysts compared to pure Co/ γ -Al₂O₃ samples. In
82 samples of high Co loadings, the spherical-shape-like morphology of the χ -phase Al₂O₃ provides
83 a better stability of the Co particles.[36]

84 This brief summary of the literature concerning Co nanoparticles on γ -Al₂O₃ and χ -Al₂O₃
85 reveals the importance of the nanoparticle-support interactions[8,17] that result from an interplay
86 between the support surface structure and its morphology. Here, we show that HRTEM and ⁵⁹Co
87 IF NMR reveal significant structural differences between the Co NPs supported on γ -Al₂O₃ and χ -
88 Al₂O₃. Finally, building on indirect DFT calculations, we link these differences to the differences
89 in initial distribution of Co precursors on the catalyst surface.

2 Experimental

2.1 Synthesis of Co/ γ -Al₂O₃ and Co/ χ -Al₂O₃ supported samples

Low-temperature metastable alumina phases were used as the supports for the studied samples. γ -Al₂O₃ was obtained by calcination of pseudoboehmite (Pural SB1, Condea Chemie, Hamburg, Germany) in air at 923 K for 6 h (1.5 K/min heating rate). The same procedure was used to obtain χ -Al₂O₃ from gibbsite (Sigma-Aldrich, Merck, Darmstadt, Germany). XRD and ²⁷Al solid-state NMR techniques (see Supplementary Materials) were used to confirm the purity of the obtained powders as in our previous works [37,38]. The resulting BET (Brunauer-Emmett-Teller) specific surface areas of γ -Al₂O₃ and χ -Al₂O₃ were roughly 175 m²/g and 150 m²/g respectively.

In order to determine the moisture capacity of the obtained supports, they were dried at a temperature of 383 K overnight. Then, droplets of distilled water were added to 1 g of alumina under continuous stirring until the sample appeared uniformly wet. The resulting values of moisture capacity were 0.91 ml/g for γ -Al₂O₃ and 0.50 ml/g for χ -Al₂O₃.

Co/Al₂O₃ supported samples with different metallic Co content were obtained using incipient wetness impregnation with an aqueous solution of Co(NO₃)₂·6H₂O (98%, Sigma-Aldrich). The higher moisture capacity of γ -Al₂O₃ allowed introducing up to 10 wt.% of Co into the sample with a single impregnation, while χ -Al₂O₃ was able to take only up to 5 wt.% Co in a single impregnation step. Thus, to obtain comparable samples with similar impregnation protocols (meaning having the same Co content obtained by following identical impregnation protocols), 5 wt.% was finally chosen as the target Co content that could be obtained for both supports in a single impregnation step. The samples were impregnated with the Co nitrate solution, then dried at 383 K for 4 hours and calcined in an Ar flow at 623 K for 4 hours. Finally, the samples were reduced in a H₂ stream (50 ml/min) at 673 K for 4 hours (3 K/min ramping rate), purged with Ar for 20 min and sealed in airtight glass ampoules to avoid oxidation. The resulting samples were denoted as 5% Co/(γ -Al₂O₃ or χ -Al₂O₃).

2.2 Characterization techniques

The morphology of the Co nanoparticles was controlled using high-resolution transmission electron microscopy (HRTEM) experiments conducted on a JEM-2010 electron microscope (Jeol, Japan) with acceleration voltage of 200 kV and 0.194 nm spatial resolution. High-angle annular dark field scanning transmission electron microscopy (HAADF-STEM) and elemental mapping images were recorded with 200 kV acceleration voltage using a JEM-2200FS electron microscope (Jeol, Japan) equipped with a Cs corrector. Particle sizes were analyzed using FIJI software.

123 ^{59}Co internal field NMR (^{59}Co IF NMR) spectra were recorded at 30 K on an AVANCE III
124 500 Fourier NMR spectrometer (Bruker, USA) using a laboratory-made solid-state probe designed
125 for low-temperature (liquid helium cooling) IF NMR experiments. The probe was operated outside
126 the magnet since IF NMR does not require an external static field. A solid-echo pulse sequence θ -
127 τ - θ was used, with a θ pulse length of 1 μs and an interpulse delay τ of 8 μs . Due to the intrinsically
128 short T_1 nuclear spin relaxation time in ferromagnetic materials, a 33 ms delay between the echo
129 sequences was used. In order to cover the entire frequency range, the spectra were recorded
130 stepwise with 500 kHz carrier frequency steps. A custom automatic tuning and matching device
131 was used to retain a constant quality factor over the entire recording range. In order to determine
132 the intensity of the spectrum at a chosen frequency, the echo signal recorded at this frequency was
133 Fourier-transformed with adequate phase and baseline corrections such that a purely absorption
134 spectrum was obtained. Then, the obtained signal was integrated over a roughly 400 kHz frequency
135 range centered at the carrier frequency, after which the value of the integral was assigned as the
136 intensity of the spectrum at said frequency. Radiofrequency irradiation power was varied at each
137 frequency step to be able to account for the differences of enhancement factors between the bulk
138 of the magnetic domains and the domain walls according to the method originally described by
139 Panissod et al. [39]

140 ^1H NMR spectra of the alumina supports were recorded at room temperature using a pulsed
141 NMR spectrometer Bruker Avance 400 with a constant magnetic field of 9.4 T (400.13 MHz ^1H
142 Larmor frequency). Prior to the ^1H NMR experiments, the samples were dehydrated for 4 hours at
143 450 $^\circ\text{C}$ and sealed inside glass ampoules to avoid rehydration from air. The samples were
144 transferred into standard 4 mm ZrO_2 rotors under argon atmosphere right before the experiment.
145 The spectra were recorded under magic angle spinning condition (MAS, 10 kHz rotation
146 frequency) using a single $\pi/2$ pulse (5 μs pulse length). 1024 scans were accumulated with a 5
147 second delay. Tetramethylsilane was used as an external reference with a chemical shift of 0 ppm.

148 **2.3 Theoretical calculation details**

149 To characterize the hydroxyl coverage of the alumina surfaces, we have conducted DFT
150 calculations of ^1H NMR chemical shifts of hydroxyl groups on the two most prominent crystal
151 planes dominating the surfaces of $\gamma\text{-Al}_2\text{O}_3$ (the (110) plane) and $\chi\text{-Al}_2\text{O}_3$ (the (111) plane)
152 according to the cubic spinel model of the metastable alumina building blocks.

153 All calculations were performed using the CASTEP program.[40] The interactions between
154 the core ions and the valence electrons were described using the projector augmented wave (PAW)
155 pseudopotentials.[41] The geometry calculations were performed at Γ point with the exchange-

156 correlation functional PW91.[42] A plane wave basis set cut-off energy of 450 eV with the self-
157 consistent field threshold of 10^{-6} eV was used. The geometry calculations used the BFGS
158 (Broyden–Fletcher–Goldfarb–Shanno) algorithm.[43]

159 To mimic a flat alumina surface, a layer of alumina was created from the spinel structure
160 with the lattice parameter a of 8.08534 Å. A model bulk crystal cell was cleaved along the (110)
161 and the (111) crystallographic planes. The (110) cell dimensions were 22.8688×16.1706 Å, while
162 the (111) cell was 19.8048×11.4344 Å. The slab thickness was varied from cell to cell, from 3.5
163 to 8 Å, with vacuum spans of more than 10 Å to prevent periodic interaction. No additional
164 restrictions were imposed during the structural relaxation. Extra hydroxyl groups were added to
165 the surface Al sites in order to avoid dangling bonds and maintain electroneutrality.

166 The ^1H NMR parameters were computed by the GIPAW method [44] with cutoff energy of
167 600 eV and PBE (Perdew-Burke-Ernzerhof) functional.[45] The ultrasoft pseudopotentials are the
168 ones supplied with CASTEP.[46].

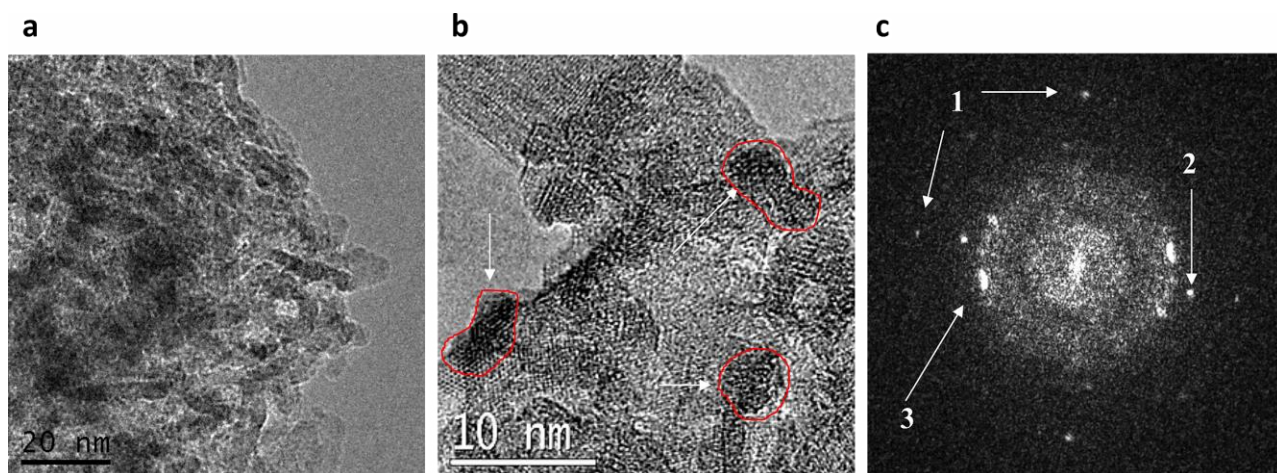
169

170 **3 Results**

171

172 **3.1 High-resolution transmission electron microscopy and EDS**

173 Figure 1 (**a**, **b**) displays typical HRTEM images of the sample 5% Co/ γ -Al₂O₃ at different
174 magnifications. According to the micrographs, the γ -Al₂O₃ support consists of large (1 μm)
175 agglomerates of randomly oriented alumina nanocrystallites that are slightly elongated along the
176 [100] axis. Cobalt nanoparticles (shown with white arrows in Fig. **1b**) are poorly distinguished on
177 the micrographs due to their relatively small size (5.5 nm mean diameter according to HRTEM
178 image analysis). Several Bragg diffraction spots, corresponding to metallic Co crystallites, are
179 clearly visible on the Fourier transform of Fig. **1b** (Fig. **1c**) along with the annular diffractions
180 from the randomly oriented crystallites of γ -Al₂O₃. Interplanar distances in *fcc* and *hcp* Co are
181 quite close, which makes the distinction between these crystal structures almost impossible here
182 despite the presence of clearly defined diffraction spots.

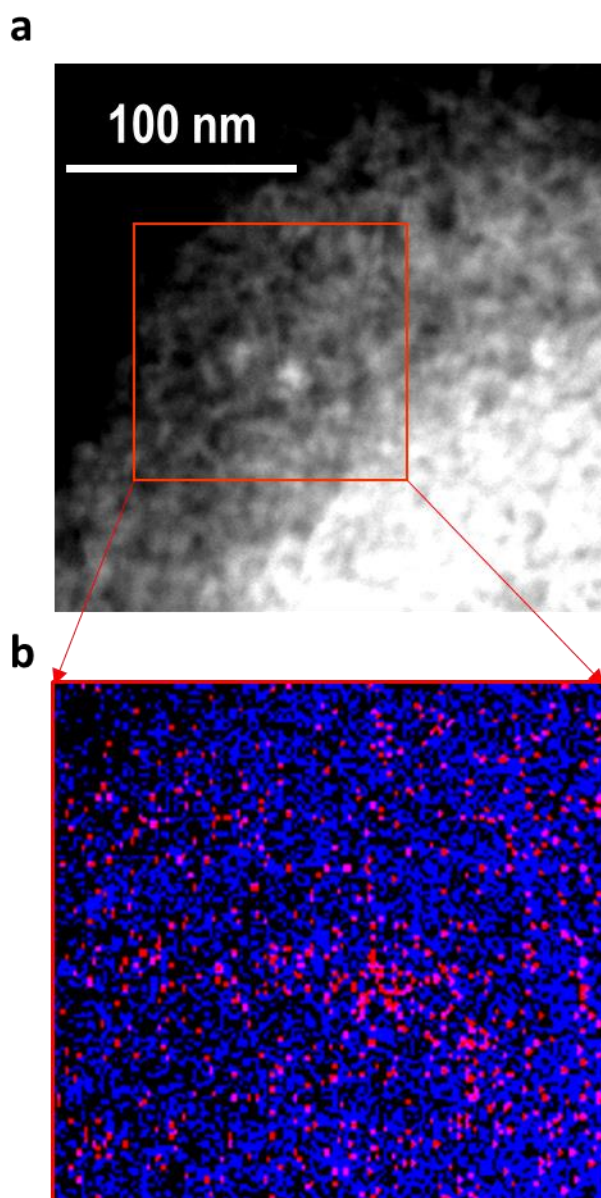


183

184 **Fig. 1.** (a) and (b): HRTEM images of the 5% Co/ γ -Al₂O₃ sample at different magnifications.
 185 Metallic Co nanoparticles are visible as dense dark areas (additionally highlighted with white
 186 arrows on b). (c): spatial Fourier transform of b), Diffraction spots shown with arrows 1 and 2
 187 correspond to cobalt nanoparticles while the annular diffractions from γ -Al₂O₃ are shown with
 188 arrow 3.

189

190 A better visualization of distribution of Co nanoparticles on the surface of the support can
 191 be obtained from the energy-dispersive mapping images recorded using HAADF-STEM technique
 192 (Fig. 2). In the corresponding EDS maps, areas where the Co K _{α 1} line (6.930 keV) emerges from
 193 the background noise are figured in red, while those where the Al K _{α 1/2} line (1.486 keV) emerges
 194 are in blue. Accordingly, Co appeared evenly distributed on the surface of the support at the spatial
 195 resolution of the HAADF-STEM image (about 1 nm) and no Co particles can be evidenced by this
 196 method.



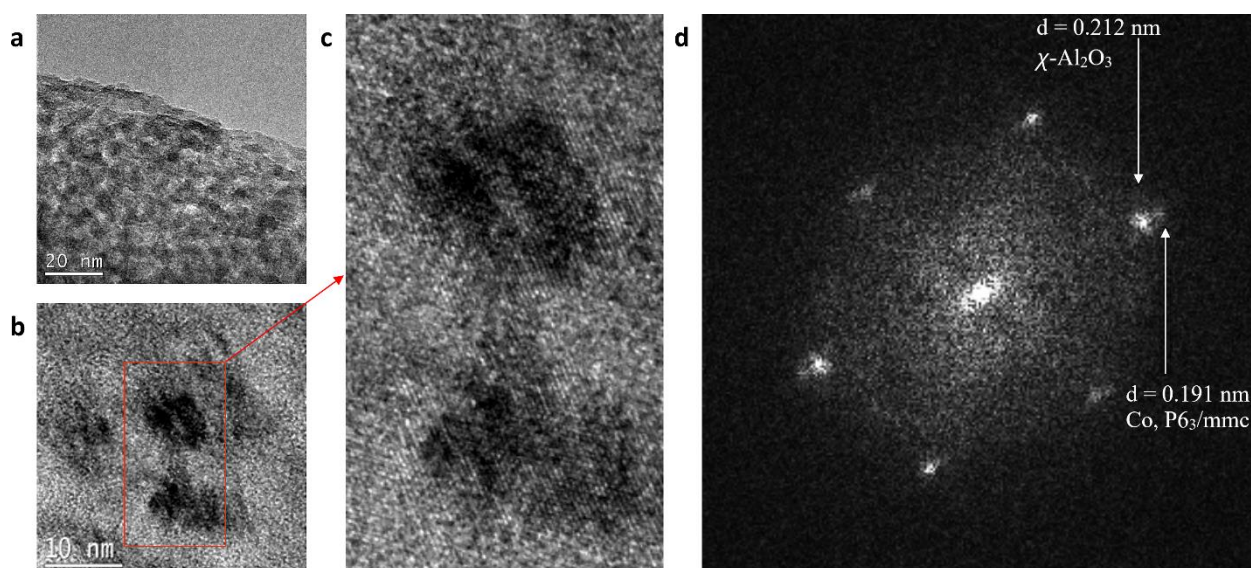
197

198 **Fig. 2.** HAADF-STEM image of the 5% Co/ γ -Al₂O₃ sample (a) and the elemental mapping of the
199 area in the red box obtained with EDS (b). Al signals are shown in blue, Co signals are shown in
200 red.

201 A significantly different picture can be seen on the HRTEM micrographs of the 5%
202 Co/ γ -Al₂O₃ sample (Fig. 3). In this case, the γ -Al₂O₃ support consists in large 0.5 μ m platelets (a
203 clear example can be seen in the HRTEM image at low magnification, Fig.S1 in Supplementary
204 Materials). The platelets are built from nanocrystalline domains (about 10x10 nm²) oriented in the
205 same direction and separated by 3-5 nm-sized pores. On this support, dark areas reveal Co
206 nanocrystallites with sizes of about 5-10 nm. Moreover, EDS images (Fig. 4b) demonstrate that
207 Co was not evenly distributed on the surface of the support. Higher Co densities areas sized up to
208 100 nm are visible and coincide with the brighter areas in the HAADF-STEM images of Figure

209 4a. Combining these observations leads to the conclusion that Co forms assemblies of ~100 nm
210 consisting of ~10 Co nanocrystallites with sizes of about 5-10 nm. In addition, the spatial Fourier
211 transform image of the micrograph containing the cobalt nanoparticles (Fig. 3d) clearly
212 demonstrates a near-overlap of the diffraction spots corresponding to the interplanar distances of
213 the support and of the metallic Co. In this FFT image the diffraction spot of Co metal ($d = 0.191$
214 nm, $P6_3/mmc$ space group, PDF №050727) is very close to the brighter diffraction spot that
215 corresponds to χ - Al_2O_3 ($d = 0.212$ nm). Together with a moiré pattern visible in the supported Co
216 nanoparticles (Fig. 3c), this signs an orientation coincidence of the Co nanocrystallite with the
217 alumina crystal domains forming the support surface. This means that both the orientation of
218 growth and the interplanar distance value coincide suggesting an epitaxial relation between the Co
219 particles and the χ - Al_2O_3 surface.

220



221

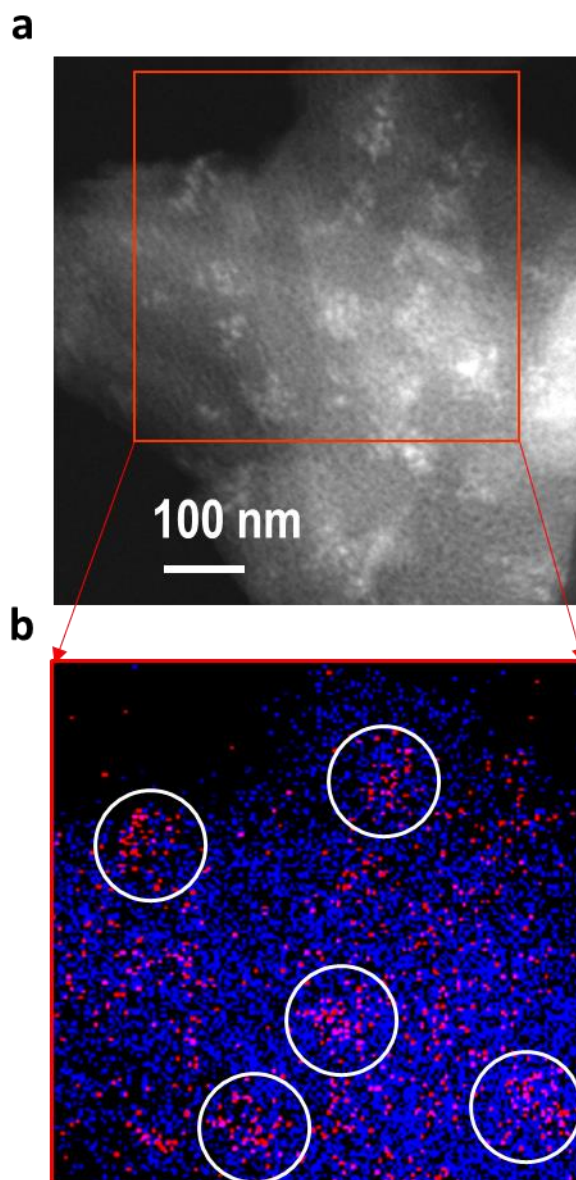
222 **Fig. 3.** (a) and (b): HRTEM images of the 5% Co/ χ - Al_2O_3 sample at different magnifications.
223 Metallic Co nanoparticles are visible as dense dark areas. (c): Magnification of the area inside the
224 red box of b). (d): Spatial Fourier transform of b). The diffraction spots corresponding to the Co
225 metal and χ - Al_2O_3 are denoted with white arrows. Such a close arrangement of diffraction spots in
226 distance and angle suggests epitaxy between the Co nanoparticle and the surface of the support.

227

228 Thus, HRTEM and HAADF-STEM techniques demonstrate that, at 5% Co loading, the χ -
229 Al_2O_3 surface appeared much more ordered than the one of γ - Al_2O_3 and that the Co nanoparticles
230 were oriented in epitaxial relation with the χ - Al_2O_3 surface. At the same time, elemental mapping
231 images show that cobalt was more homogeneously dispersed over the surface of γ - Al_2O_3 in the

232 form of small (5 nm and less) nanocrystallites, while larger Co nanocrystallites (5-10 nm) tended
233 to associate on the surface of χ -Al₂O₃.

234 Electron microscopy techniques revealed the morphology and structure of the samples, but
235 due to their strictly local character, these methods are not optimal for studying the crystal structure
236 of Co nanoparticles in the entire volume of the sample. In contrast, ⁵⁹Co internal field NMR (⁵⁹Co
237 IF NMR) is a technique able to discern between different types of crystal structure of metallic Co
238 in the bulk – something that is more likely to relate to the overall efficiency of the catalyst.



239

240 **Fig. 4.** HAADF-STEM image of the 5% Co/ χ -Al₂O₃ sample (a) and the elemental mapping of the
241 area in the red box obtained with EDS (b), Al signals are shown in blue, Co signals are shown in
242 red. White circles in (b) are used to locate the large Co NP assemblies identified as brighter areas
243 in (a). Individual points on the EDS elemental maps do not indicate the presence of Co with
244 certainty, because their appearance may be connected with the background noise in the EDX
245 spectra. However, since noise is expected to be randomly distributed on the elemental maps, the
246 areas that contain larger densities of points (shown with the white circles in Fig. 4b) can be
247 associated with Co particles and do indeed coincide with the brighter areas of the HAADF-STEM
248 image (Fig. 4a).

249

250

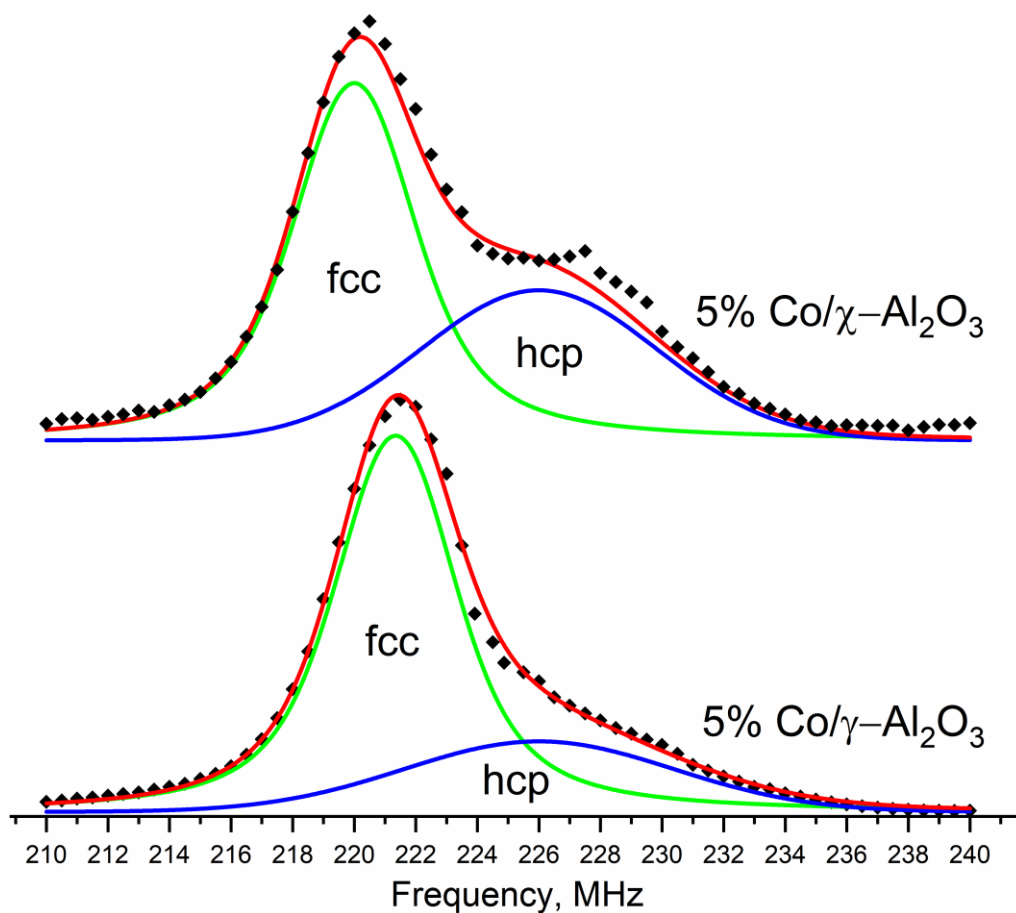
3.2 ⁵⁹Co internal field nuclear magnetic resonance

251

252 ⁵⁹Co IF NMR spectra reflect both the crystal and the magnetic structures of Co nanoparticles,
253 which affect the hyperfine magnetic field at the location of the nucleus. It can be observed only in
254 ferromagnetic particles. In superparamagnetic ones, the internal field fluctuates rapidly at the
255 timescale of the NMR experiments and no signal is generated. Consequently, we have
256 demonstrated earlier that the size of Co nanoparticles is an equally important factor affecting the
257 ⁵⁹Co IF NMR spectra, when particles below the nominal critical superparamagnetic size are
258 present in the sample and invisible in the IF NMR spectra. The critical size below which particles
259 isolated from each other are superparamagnetic (and thus are undetectable in IF NMR) at room
260 temperature was shown to be equal to roughly 7.5 nm in diameter for isolated particles.[21]
261 However, in non-isolated particles, magnetic ordering of the particles due to interparticle magnetic
262 interactions (dipolar and exchange) affects the critical size for superparamagnetic/ferromagnetic
263 transition in a way that is difficult to predict quantitatively. In practice, we can consider the
264 particles to be isolated when the energy of dipolar interaction between the particles is much smaller
265 compared to magnetic anisotropy energy[47], which is the case for cobalt particles about 5 nm in
266 diameter and separated by at least the same distance. From these considerations, according to the
267 electron microscopy data, a significant fraction of Co nanoparticles in the 5% Co/ γ -Al₂O₃ and 5%
268 Co/ χ -Al₂O₃ samples could be superparamagnetic and undetectable by ⁵⁹Co IF NMR at room
269 temperature. Therefore, we conducted the ⁵⁹Co IF NMR experiments at 30 K where the critical
270 particle size for superparamagnetic transition decreases to 3.5 nm. It can then be safely assumed
271 that almost all Co particles in the studied samples are in a ferromagnetic state and contribute to the
272 ⁵⁹Co IF NMR spectra.

273 As stated in the experimental section and according to a now well-established
274 procedure,[21] the spectra were recorded at different radiofrequency powers in order to discern
275 between the multi domain and single domain ferromagnetic particles. The distribution of optimal
276 radiofrequency power (power at which the spectral intensity at the chosen frequency is maximum)
277 for all spectra was practically uniform meaning that we have not detected any multi domain Co
278 particles. This is in complete agreement with the observations made using HRTEM since multiple
279 magnetic domains are not expected to occur in particles smaller than 70 nm.[48] Therefore, all of
280 the obtained spectra were analyzed from the standpoint of single domain particles.

281



282

283 **Fig. 5.** ^{59}Co IF NMR spectra of the 5% $\text{Co}/\gamma\text{-Al}_2\text{O}_3$ (bottom) and 5% $\text{Co}/\chi\text{-Al}_2\text{O}_3$ (top) samples. T
 284 = 30 K. Spectra are normalized to the same maximal intensity. Echo measurement points are shown
 285 with symbols, while the lines show the result spectral decomposition into two Pseudo-Voigt
 286 profiles for *fcc* Co (green) and *hcp* Co (blue). The sum of these two profiles is shown in red.

287

288 ^{59}Co IF NMR spectra of the studied samples recorded at 30 K are shown in Fig. 5. The
 289 spectrum of the sample supported on $\gamma\text{-Al}_2\text{O}_3$ (bottom) displays a dominant line centered at 222
 290 MHz that corresponds to single domain particles with *fcc* structure [26]. The relatively weak wide
 291 shoulder stretched from 224 MHz to 235 MHz indicates the minor occurrence of particles with
 292 *hcp* structure [26]. The *hcp* crystal structure is the stable form of bulk Co at, and below, room
 293 temperature (the *hcp*–*fcc* transition is known to happen at roughly 700 K). However, according to
 294 many experimental observations, the decrease of the size of Co nanoparticles leads to the
 295 stabilization of the *fcc* crystal phase to the extent that this phase becomes dominant for relatively
 296 small nanoparticles, as observed here.[49,50] Thus, the obtained spectrum further corroborates the
 297 electron microscopy observations that Co was present as highly dispersed small nanoparticles over
 298 the surface of the support in the case of $\gamma\text{-Al}_2\text{O}_3$. Tsakoumis et al. have shown using HRTEM that

299 even at a 20 wt.% Co loading, Co nanoparticles supported on the surface of γ -Al₂O₃ have an
300 average size of 5.2 nm with no particles larger than 14 nm in diameter.[8] This is consistent with
301 the observed prevalence of the *fcc* Co signal in the ⁵⁹Co IF NMR spectrum of the sample supported
302 on γ -Al₂O₃ that is reported here.

303 In the spectrum of the 5% Co/ χ -Al₂O₃ sample (Fig 5, top), one can observe a similar line
304 shape consisting of two broad signals corresponding to single domain *fcc* and *hcp* phases of Co,
305 with the *fcc* line undergoing a 1 MHz frequency shift compared to the 5% Co/ γ -Al₂O₃ sample. The
306 quantitative analysis of the *fcc* and *hcp* fractions in the samples can be made by decomposition of
307 the experimental spectra into two broad peaks. The signal from the *fcc* and *hcp* packed Co can be
308 represented as two Pseudo-Voigt profiles centered around 220 MHz and 227 MHz respectively,
309 with the line for *hcp* Co being much broader than the line of *fcc* Co due to stronger magnetic
310 anisotropy in the former case [51]. The end results of such decomposition (shown as colored lines
311 in Fig. 5), namely the relative intensities of the *fcc* and *hcp* signals, reflect the relative contents of
312 these crystal phases in the samples, which were 24% of *hcp* Co for γ -Al₂O₃ and 39% *hcp* Co for χ -
313 Al₂O₃. Those values constitute a lower estimate. Indeed, very small *fcc* Co particles being
314 superparamagnetic might not contribute to the IF NMR spectra.

315

3.3 Experimental and predicted ^1H chemical shifts

The initial stage in the formation of Co nanoparticles on the surface of the support is the anchoring of Co(II), from the precursor ions, on the available vacant sites. Using EXAFS and *ab initio* calculations of the adsorption energy of Co on different surfaces of $\alpha\text{-Al}_2\text{O}_3$, Chizallet et al. [52] have recently demonstrated that the hydroxyl coverage of the surface and the location of the surface vacancies greatly influence the interaction energy of Co(II) with the alumina surface.

Determining *ab initio* the hydroxyls on the alumina surface susceptible to interaction with different amounts of Co(II) is obviously very informative but requires lengthy computations involving large sets of models with different types of alumina surfaces together with the necessary water to coordinate and stabilize the dangling groups. We tried instead a semi empirical approach based on correlating of the experimentally observed and theoretically predicted ^1H NMR shifts.

To that aim, the first step is to choose a reliable structural model of $\gamma\text{-Al}_2\text{O}_3$ and $\chi\text{-Al}_2\text{O}_3$ surfaces. While modelling the surface of the stable trigonal α -alumina is relatively straightforward due to its completely refined crystal structure, the structures of metastable alumina remain disputed. In particular, the low temperature $\gamma\text{-Al}_2\text{O}_3$ metastable phase has attracted the highest attention due to its relevance as a heterogeneous catalyst and catalyst support. $\gamma\text{-Al}_2\text{O}_3$ is generally considered to have a cubic spinel structure [29,53], even though the stoichiometry of Al_2O_3 does not directly correspond to a spinel AB_2O_4 . Such structural disparity led to different models describing the distribution of Al ions and vacancies in the spinel cationic sublattice [29]. Despite the differences of these models, the majority of researchers agree that the bulk structure of $\gamma\text{-Al}_2\text{O}_3$ particles belongs to the cubic spinel type. On the other hand, the surfaces structure and bonding scheme of these particles remain debated and a brief discussion of existing models is necessary before proceeding further.

The most widely used models of metastable alumina surfaces were proposed by Knözinger and Ratnasamy [54]. It consists of bulk spinel structure cleavages along (100), (110) and (111) crystal planes. The reactivity of such surfaces in hydrated conditions then mainly depends on the hydroxyl coverage obtained by addition of protons and hydroxyls to compensate for the charge and coordination symmetry of surface Al and O sites [55,56]. Further improvements upon this model include reconsiderations of the bulk alumina structure to non-spinel models [57], as well as accounting for the finite size effect [58,59] and for stacking faults of individual alumina crystallites [30].

The first implication of the finite size of an alumina crystallite is the presence of edges between its surfaces that leads to the occurrence of unique hydroxyl sites that are not hydrogen-

349 bonded to other hydroxyl groups and remain highly reactive to chlorination as was shown by ^1H
350 NMR and *ab initio* calculations by Batista et al. [58]. The second important effect of the finite
351 particle size is connected to the synthetic routes used to obtain the metastable aluminas. Most
352 frequently, aluminum oxides are obtained through dehydration of corresponding hydrates as was
353 experimentally demonstrated by Stumpf et al [60]. In this case, the restructuring of individual
354 particles is governed by topotactic transformations during which the structural features of the
355 initial particles are conserved. Due to the layered nature of the alumina hydrates, the topotactic
356 transitions result in differences between alumina surfaces that formally belong to the same crystal
357 plane family (e. g. (110) cubic spinel plane) depending on basal/lateral position in the initial
358 particle as was demonstrated using DFT calculations in the recent paper by Pigeon et al. [59].

359 At the same time, metastable aluminas are intrinsically nanostructured materials, thus the
360 description of their structures requires to account for the defectiveness and stacking of the
361 individual crystallites that also play an important role on the formation of the particle surfaces.
362 The approach developed by Tsybulya et al. accounts for the connectivity of individual spinel
363 crystallites through planar defects lying in the (100), (110) and (111) crystal planes of cubic spinel
364 [30]. This technique allowed modeling the structures of low-temperature aluminas as well as
365 demonstrating the effect of abundant shearing planar defects that allow the existence of a cubic
366 spinel material with a non-spinel stoichiometry. Later, this approach was also used by
367 Pakharukova et al. to create 3D nanostructured models of $\gamma\text{-Al}_2\text{O}_3$ particles and simulate the XRD
368 patterns, which coincide with experimental XRD patterns and allow to explain the diffuse nature
369 of several peaks [61].

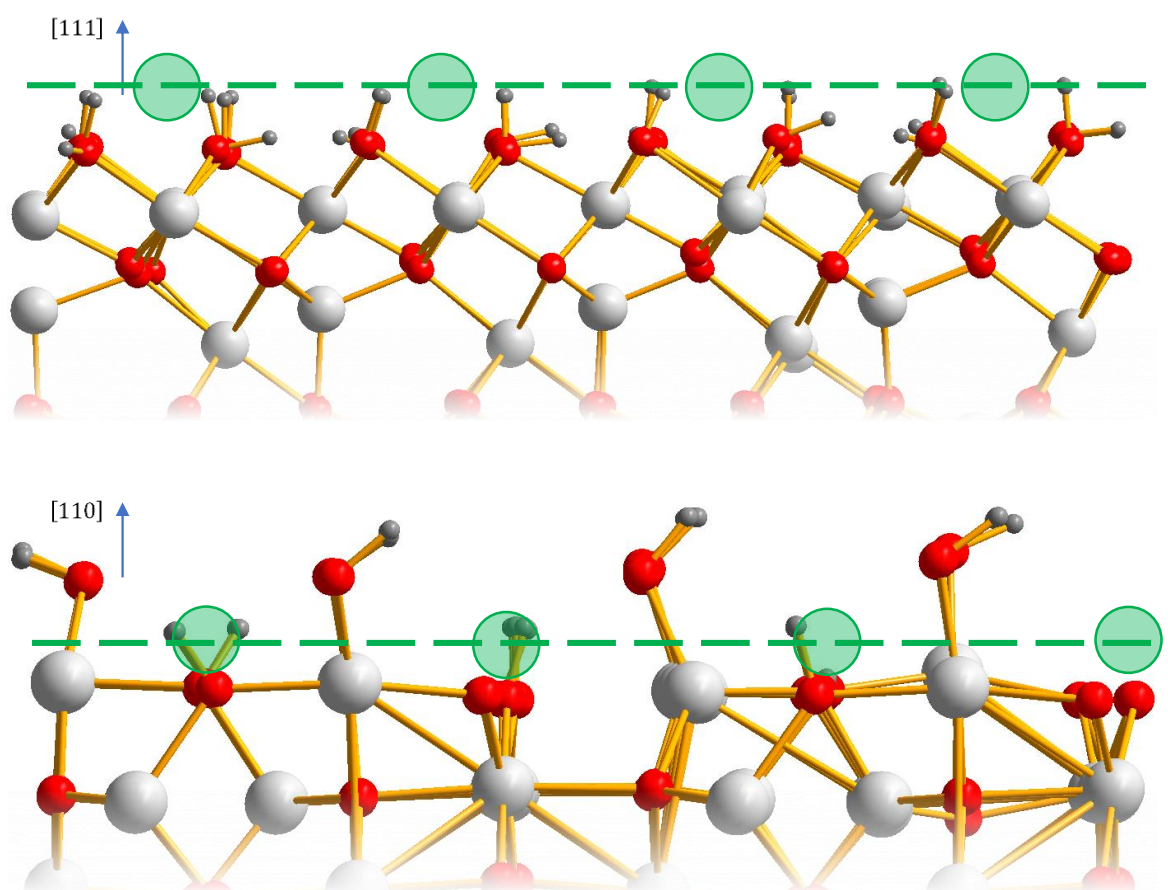
370 Both the topotactic transition and crystallite stacking approaches do not contradict each
371 other, but provide a complementary description of both the bulk and the surface of metastable
372 alumina nanoparticles. Importantly, both of these approaches coincide in their prediction of the
373 crystal planes that form the surface of $\gamma\text{-Al}_2\text{O}_3$ nanoparticles, namely (100) and (110) crystal planes
374 with the minor presence of the (111) plane.

375 The much less investigated structure of the metastable $\chi\text{-Al}_2\text{O}_3$ obtained through
376 dehydration of aluminum trihydroxide gibbsite remains an open question without any commonly
377 accepted viewpoint. The source of this controversy lies in the presence of a diffuse scattering peak
378 at $2\theta = 43^\circ$ in its XRD pattern that does not belong to the cubic spinel structure, even though the
379 rest of the XRD pattern corresponds to the said structure. Additionally, the ^{27}Al NMR spectra
380 reveal an $\text{Al}^{[6]}:\text{Al}^{[4]}$ equal to roughly 3:1, that also does not correspond to the spinel structure, for
381 which this ratio is expected to be 2:1 (as observed in ^{27}Al NMR spectra of $\gamma\text{-Al}_2\text{O}_3$) [62]. However,
382 recently, Yatsenko et al. [63] have shown using the “crystallite stacking” approach that the non-

383 spinel diffuse scattering peak of χ -Al₂O₃ may appear due to planar defects of the anion sublattice
384 of cubic spinel structure (the O²⁻ sublattice in ratio AB₂O₄ spinel follows a regular *fcc* pattern, while
385 such planar defects change its local ordering to *hcp*). This observation allows one to consider the
386 particles of χ -Al₂O₃ as having the cubic spinel structure when trying to model its surface in the
387 same way as it was done for γ -Al₂O₃. With this consideration, the surface of χ -Al₂O₃ is mostly
388 represented by the (111) spinel crystal plane as was shown in [30]. Moreover, if we apply the same
389 logic of topotactic transitions to the well-refined structure of gibbsite just as it was done for
390 boehmite in the case of γ -Al₂O₃, the result for the most exposed crystal plane will be the same.
391 Indeed, the hexagonally symmetric particles of gibbsite have a layered structure with the layers of
392 aluminum octahedral separated by hydrogen-bonded hydroxyl layers in the direction perpendicular
393 to the [001] axis. Thus, the (001) crystal plane that has a hexagonal symmetry is the most prevalent
394 for the gibbsite particles [64,65]. According to Mitsui et al. [66], gibbsite particles retain their
395 morphology during the dehydration into χ -Al₂O₃ including the hexagonal symmetry of the (001)
396 basal planes. Therefore, the retention of the particle morphology and the surface prevalence of the
397 hexagonally symmetric planes (001) in the case of gibbsite and (111) in the case of χ -Al₂O₃ allow
398 us to assume that the (001) basal planes of gibbsite undergo a transition into the (111) planes of
399 the dehydrated alumina.

400 In summary, the surface of metastable aluminas can be accurately described in terms of
401 spinel crystal planes, mainly (100) and (110) with the minor presence of the (111) for γ -Al₂O₃
402 nanoparticles, and (111) for χ -Al₂O₃.

403 Accordingly, the γ - and χ -Al₂O₃ surfaces (Fig. 6) were modeled by cleaving the crystal
404 structure along the directions of the (110) or (111) crystal planes. We also note that such a
405 representation of the particle surface as infinite slab cannot possibly account for the edges formed
406 between the crystallite surfaces or for the subtle features of the crystal planes formed during the
407 topotactic transition. Nevertheless, such approach can still be feasible and useful for the prediction
408 of the general behavior of the alumina surface towards the hydrated Co ions in the precursor
409 solution. By using the similar infinite slab model, Larmier et al. [17] have demonstrated the so-
410 called structural recognition of Co²⁺ ions on the (100) and (110) surfaces of a cubic spinel model
411 of γ -Al₂O₃. They have shown that the most energetically favorable mode of adsorption of Co²⁺
412 ions is the one during which octahedral complexes including one or two bonds between Co²⁺ and
413 lattice oxygen are formed.



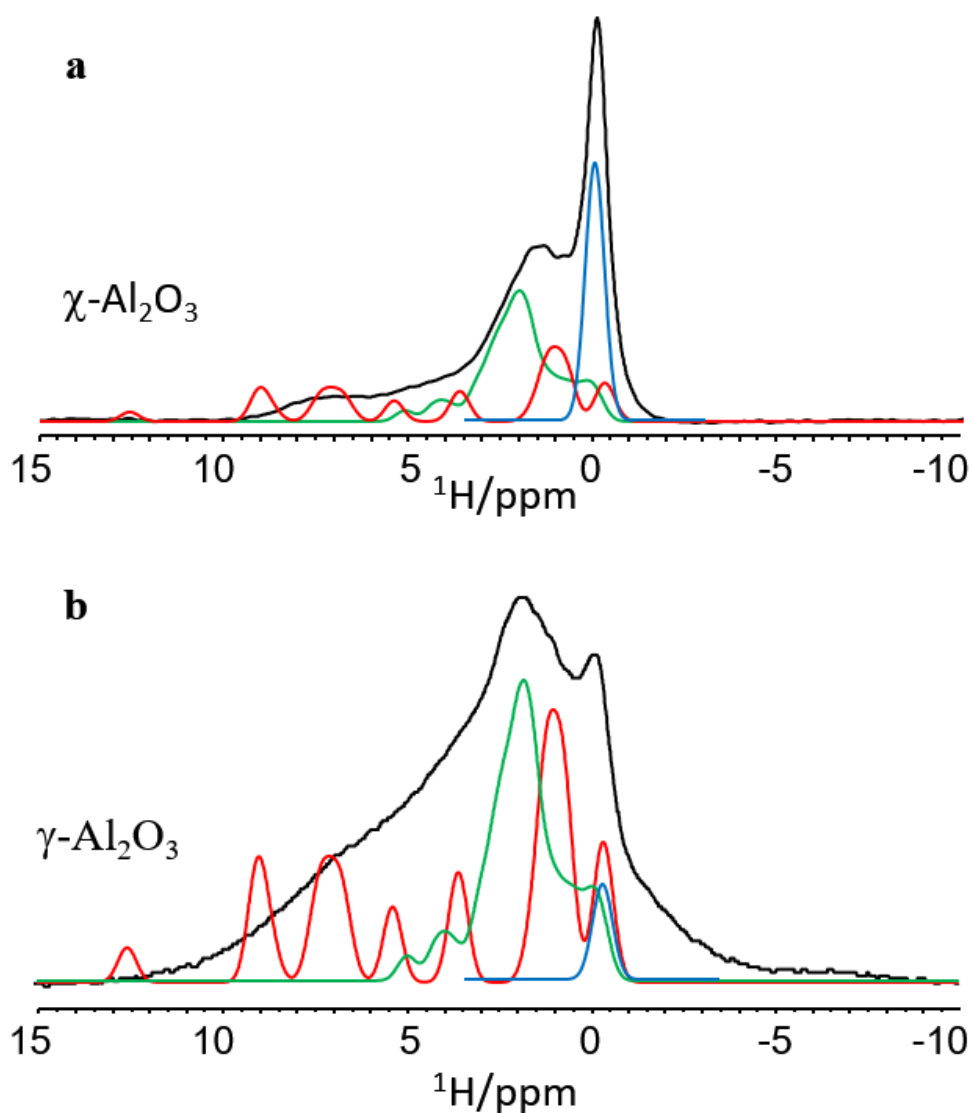
414

415 **Fig. 6.** Models of the (111) (top) and (110) (bottom) crystal planes of the spinel structure
 416 of crystallites forming metastable alumina phases. Al atoms are shown in silver, O atoms are
 417 shown in red, H atoms are shown in black. Green circles and lines denote the positions of the Al
 418 atoms that are missing from the next layer. Such sites can form vacancies available to Co^{2+} ions.

419

420 The hydroxyl groups were added to the spinel slabs to compensate for the charge and any
 421 dangling bonds that were formed during the cleavage (more details can be found in the
 422 Experimental section). After the relaxation of the structures without any additional constraints, we
 423 calculated the ^1H chemical shifts of all the hydroxyl groups now present on these model surfaces.
 424 The resulting sets of calculated chemical shifts ascribed to the (110) and (111) surfaces, as well as
 425 their comparison with the experimental ^1H NMR spectra, can be found in Fig. 7 (calculated spectra
 426 are shown with colored lines, while the experimental data are shown in black). Both the calculated
 427 sets of chemical shifts and the experimental ^1H 10 kHz MAS NMR spectra displayed a significant
 428 difference in the spectral intensity in the 5-10 ppm region. Namely, the intensity in this region was
 429 zero for the (111) plane model, which agreed well with the low relative intensity observed in the
 430 same region of the experimental spectrum of $\chi\text{-Al}_2\text{O}_3$. Furthermore, edges between the spinel
 431 surfaces are present in both samples, resulting in additional terminal hydroxyl groups that give rise

432 to a distinct line at 0 ppm in the experimental spectra (blue line in Fig. 7**a, b**) as was predicted by
433 Batista et al. [58]. These hydroxyl groups were obviously missing from the perfect plane models
434 and thus, had to be added to the decomposition of the experimental spectra manually. The
435 experimental spectra were decomposed into the theoretical spectra for (111) and (110) planes as
436 well as the line corresponding to surface edges until the best match was achieved. The resulting
437 relative intensities of the theoretical spectra of crystal planes excluding the surface edges were:
438 50% (111) plane and 50% (110) plane for χ -Al₂O₃; 30% (111) plane and 70% (110) plane for γ -
439 Al₂O₃. Thus, the ¹H NMR data demonstrate that the surface of γ -Al₂O₃ is mostly represented by
440 the (110) crystal plane, while an equal mixture of (111) and (110) spinel crystal planes makes up
441 the surface of χ -Al₂O₃. The difference between the compositions of these surfaces can play an
442 important role during their interaction with the Co impregnation solution since hydroxyl coverages
443 of the spinel crystal planes differ significantly: the hydration of the (111) spinel plane gives rise
444 exclusively to bridging (μ_2 - and μ_3 -OH) groups, while the (110) spinel plane contains a mixture of
445 terminal (μ_1 -OH) and bridging (μ_2 -OH) groups.



446

447 **Fig. 7.** Decomposition of the experimental 10 kHz MAS ^1H NMR spectra of dehydrated $\chi\text{-Al}_2\text{O}_3$
 448 (a, black line) and $\gamma\text{-Al}_2\text{O}_3$ (b, black line) into the theoretically calculated spectra for (110) and
 449 (111) spinel planes (red and green lines, respectively) and the separate line corresponding to
 450 hydroxyl groups supported on the edges between the crystallite surfaces according to ref. [58]
 451 (blue line). The relative contributions of the (111) and (110) planes to the spectra excluding the
 452 signal at 0 ppm, were: 50% (111) plane and 50% (110) plane in the case of $\chi\text{-Al}_2\text{O}_3$; 30% (111)
 453 plane and 70% (110) plane in the case of $\gamma\text{-Al}_2\text{O}_3$. Note, that the given values reflect the surface
 454 densities of the OH groups and correspond directly to the surface areas represented by these planes
 455 in the samples.

456

4 Discussion

Larmier et al. have shown, using DFT calculations, that epitaxial interaction of aqueous cobalt precursor with the surface of γ -Al₂O₃ (modelled as (100) and (110) infinite cleaved slabs) is energetically favorable during the impregnation and drying stages of FTS catalyst synthesis.[17] This interaction was linked to the formation of the mixed cobalt-aluminum oxide layer at the interface between the support surface and Co nanoparticle through structural recognition. Simply put, Co²⁺ ions from the impregnation solution tend to occupy the vacancies created by removal of the octahedral Al³⁺ sites, which leads to creation of stable octahedral Co²⁺ complexes and dispersion of Co over the surface of the support. This, in turn, may lead to the deactivation of small (less than 5.3 nm in diameter) Co nanoparticles during the onset of FTS or a complete inactivity of the sample in the extreme case of very small (less than 3 wt.%) Co loading [8].

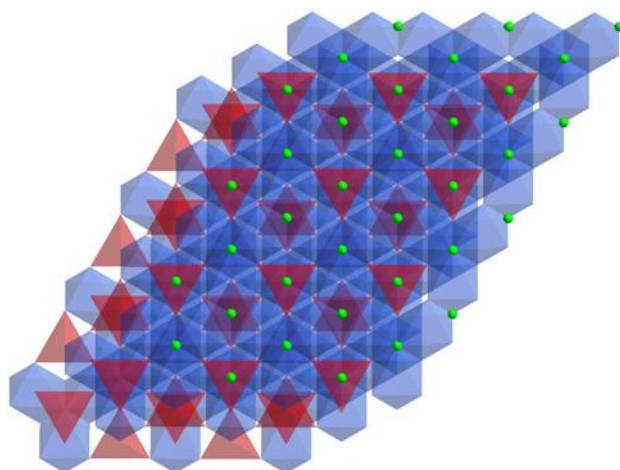
The epitaxial relation between the reduced Co nanoparticles and the surface of χ -Al₂O₃ that we observed by HRTEM in the reduced sample was necessarily a direct consequence of a strong particle-support interaction at some stage of the synthesis. However, the effects of this interaction were strikingly different in the cases of γ - and χ -Al₂O₃. The key differences between these supports lie firstly in the crystal planes dominating their surface and secondly in the morphology of the particles.

As apparent from our semi empirical modelling of alumina surfaces, γ - and χ -Al₂O₃ differ by the nature of crystal planes at their surface thus leading to completely different types of hydroxyl coverage. The hydroxyl coverage of (111) plane (and correspondingly χ -Al₂O₃, Fig. 6 top) consists exclusively of bridging hydroxyl groups located under the potential vacancies (missing Al³⁺ sites, shown with green circles in Fig. 6, top), thus preventing them from stabilizing any adsorbed ion. For the (110) plane (dominating the surface of γ -Al₂O₃, Fig. 6 bottom) we observe a picture strongly resembling the C- μ_1 - μ_2 model presented by Chizallet et al. [52], with the main similarity being the mixed terminal-bridging hydroxyl coverage. This, in turn, is connected with the presence a plane below the level of terminal hydroxyl where vacancies for octahedral complexes can form and provide direct anchoring to the lattice O²⁻ (Fig. 6, bottom). According to DFT calculations made by Chizallet et al., these vacancies provide a large gain in the absorption energy during the onset of Co(OH)₂ formation. Such increased strength of interaction between the metallic Co precursor and the surface of the support would inevitably lead to strong dispersion of Co²⁺ ions over the surface of γ -Al₂O₃ that would in turn result in a large amount of hard-to-reduce Co species and a decrease of the metallic Co particle size. A prominent signal at 0 ppm in the ¹H NMR spectrum of χ -Al₂O₃ is also worth noting because according to

491 work by Batista [58] this chemical shift range corresponds to the hydroxyl groups supported on
492 the edge between the crystallite surfaces of the particle. Thus, even though the relative content of
493 these hydroxyl groups is high, they do not facilitate the anchoring of the Co^{2+} ions due to their
494 location. Indeed, the edges contain undercoordinated sites and cannot provide a suitable vacancy
495 for an octahedral Co^{2+} complex.

496 Thus, the modeling of the hydroxyl coverage helps rationalize the observations made using
497 HRTEM and ^{59}Co IF NMR; namely, the smaller particle size and the prevalence of *fcc* metallic
498 Co in the sample supported on $\gamma\text{-Al}_2\text{O}_3$ after calcination and reduction, when compared to the
499 sample supported on $\chi\text{-Al}_2\text{O}_3$. The same rationalization may also be made for the difference in
500 moisture capacities that we observed during the sample preparation while the specific surface areas
501 of the powders were very close. The role of surface hydroxyl coverage during surface wetting has
502 been studied for many oxide materials including Al_2O_3 [67,68]. Dangling hydroxyl groups
503 available for the formation of H-bonds with the water molecules were shown to facilitate the
504 formation of a liquid water layer on the surface of all of the studied oxides. Thus, the higher
505 moisture capacity of $\gamma\text{-Al}_2\text{O}_3$ can also be ascribed to the presence of terminal hydroxyl groups on
506 (110) plane representing the majority of its surface.

507 Furthermore, the remarkable coincidence of the structural parameters of the metallic Co
508 particles and the surface of $\chi\text{-Al}_2\text{O}_3$ cannot be ignored here. The hexagonally symmetric pattern of
509 its surface may be directly rationalized through topotactic transformations of gibbsite particles as
510 was mentioned above. This direct observation of the prominent (111) crystal plane in HRTEM
511 images of $\chi\text{-Al}_2\text{O}_3$ serves as a further proof for the spinel-based models of its crystal structure and
512 may shed light on what can be called structural recognition in this case. In the view of the (111)
513 surface model presented in the preceding section, it can be inferred that the missing Al atoms
514 (possible vacant sites for Co^{2+} anchoring) also follow a hexagonal pattern. Moreover, the
515 morphology of $\chi\text{-Al}_2\text{O}_3$ particles that includes relatively large and oriented crystallites would favor
516 the formation of larger and well-ordered metal particles. However, the distance between any two
517 closest "vacancies" (approximately 4.5 Å) is much larger than the Co-Co distance in the metallic
518 cobalt (approximately 2.5 Å). Consequently, we cannot say that this simple vacancy model
519 determines the way in which the Co nanoparticles are formed after reduction. Nevertheless, it is
520 reasonable to assume that the hexagonal symmetry of the surface of $\chi\text{-Al}_2\text{O}_3$ promotes the *hcp*
521 phase formation who appeared favored from the experimental NMR observations.



522

523 **Fig. 8.** View on the (111) plane from the above. Tetrahedral Al sites are depicted with red,
524 octahedral Al sites are depicted with blue. Green dots represent the possible vacancies.

525

526 **5 Conclusions**

527

528 Rational design of supported cobalt catalysts requires an efficient way to predict the catalytic
529 properties of Co nanoparticles based on their structural and morphological properties. Such
530 predictions are made possible by the extensive studies on the influence of Co NP sizes and
531 crystalline structures on their activity and selectivity. In this work, the application of a non-local
532 technique such as ^{59}Co Internal Field NMR spectroscopy in combination with local electron
533 microscopic techniques proved to be very efficient. It provided an efficient way to investigate the
534 structure and size (partially through the dependence on the stability of different crystal structures
535 on the size of the nanoparticles) of the cobalt nanoparticles on the surface of the sample.

536 In particular, we have demonstrated that $\chi\text{-Al}_2\text{O}_3$ makes more favorable the *hcp* structure for
537 supported Co metal nanoparticles, which is related to the presence of larger particles when
538 compared to the ones supported on $\gamma\text{-Al}_2\text{O}_3$, as revealed by 30 K ^{59}Co NMR experiments.
539 Correspondingly, the elemental mapping performed during the STEM experiments revealed the
540 presence of 5-10 nm metallic Co particles assembled into patches on the surface of $\chi\text{-Al}_2\text{O}_3$ in
541 contrast to highly dispersed Co on the surface of $\gamma\text{-Al}_2\text{O}_3$. Such a difference between these
542 metastable alumina phases could be attributed to the alumina particle morphologies observed in
543 HRTEM micrographs. $\gamma\text{-Al}_2\text{O}_3$ formed aggregates of small randomly oriented nanocrystallites,
544 while the $\chi\text{-Al}_2\text{O}_3$ sample consisted of larger micron-sized plates oriented in the same crystalline
545 direction that gave rise to a hexagonal pattern of diffraction spots in the Fourier transform analysis.
546 Such particle morphologies, together with the slightly smaller specific surface area of $\chi\text{-Al}_2\text{O}_3$,

547 would naturally lead to larger Co particles reduced on this support. Additionally, in agreement
548 with the works by Chizallet et al.[52] and Larmier et al. [17], the hydroxyl coverage of Al₂O₃
549 plays an important role in the formation of Co particles by creating vacant sites that can
550 accommodate an octahedral Co²⁺ complex anchored directly to the O²⁻ sublattice.

551 According to the approach developed by Tsybulya, different metastable aluminas consist of
552 similar spinel blocks but stacked in different ways, the crystal planes most prominent on the
553 surface of their particles also differ. This allowed us to create simple models of χ -Al₂O₃ and
554 γ -Al₂O₃ surfaces, and in particular of their hydroxyl coverages. As we confirmed using ¹H MAS
555 solid-state NMR and *ab initio* DFT calculations of ¹H chemical shifts, the (111) crystal plane
556 representing the surface of χ -Al₂O₃ contained exclusively bridging hydroxyl groups, while the
557 (110) crystal plane prominent in γ -Al₂O₃ contained a mixture of bridging and terminal hydroxyls.
558 According to the literature, the presence of both types of hydroxyl groups facilitates both the
559 wetting of the surface and the dispersion of Co cations over the surface of the support. This, in
560 turn, would facilitate the dispersion of metallic Co apparent in 5% Co/ γ -Al₂O₃ sample.

561 This is in complete agreement with our experimental observations by HRTEM and IF NMR
562 of larger hcp Co particles on χ -Al₂O₃. The structure and particle morphology of χ -Al₂O₃ led to the
563 formation of larger Co nanoparticles with higher *hcp* Co content as compared to γ -Al₂O₃. The hcp
564 Co structure is further stabilized by the hexagonal symmetry of the (111) spinel crystal plane.
565 Thus, the type of the surface of the alumina support can influence the size and crystal structure of
566 the supported Co nanoparticles, which provides further possibility for deposition of Co
567 nanoparticles with the desired catalytic properties.

568 **6 Acknowledgements**

569

570 The reported study was funded by RFBR according to the research project No. 20-33-90184.
571 This work was partially supported by the Ministry of Science and Higher Education of the Russian
572 Federation within the governmental order for Boreskov Institute of Catalysis (project AAAA-A21-
573 121011390054-1). NMR equipment at ESPCI Paris is funded in part by the Paris Region. I.V.Y.
574 benefited from the Vernadski PhD fellowship from the French Embassy in Moscow.

575

7 References

- 578 [1] T.W. van Deelen, C. Hernández Mejía, K.P. de Jong, Control of metal-support
579 interactions in heterogeneous catalysts to enhance activity and selectivity, *Nat*
580 *Catal.* 2 (2019) 955–970. <https://doi.org/10.1038/s41929-019-0364-x>.
- 581 [2] O. Ducreux, B. Rebours, J. Lynch, M. Roy-Auberger, D. Bazin, Microstructure
582 of Supported Cobalt Fischer-Tropsch Catalysts, *Oil & Gas Science and*
583 *Technology - Revue de l'IFP.* 64 (2009) 49–62.
584 <https://doi.org/10.2516/ogst:2008039>.
- 585 [3] D.I. Enache, B. Rebours, M. Roy-Auberger, R. Revel, In Situ XRD Study of the
586 Influence of Thermal Treatment on the Characteristics and the Catalytic
587 Properties of Cobalt-Based Fischer–Tropsch Catalysts, *Journal of Catalysis.*
588 205 (2002) 346–353. <https://doi.org/10.1006/jcat.2001.3462>.
- 589 [4] H. Karaca, O. V. Safonova, S. Chambrey, P. Fongarland, P. Roussel, A.
590 Griboval-Constant, M. Lacroix, A.Y. Khodakov, Structure and catalytic
591 performance of Pt-promoted alumina-supported cobalt catalysts under realistic
592 conditions of Fischer–Tropsch synthesis, *Journal of Catalysis.* 277 (2011) 14–
593 26. <https://doi.org/10.1016/j.jcat.2010.10.007>.
- 594 [5] M.K. Gnanamani, G. Jacobs, W.D. Shafer, B.H. Davis, Fischer–Tropsch
595 synthesis: Activity of metallic phases of cobalt supported on silica, *Catalysis*
596 *Today.* 215 (2013) 13–17. <https://doi.org/10.1016/j.cattod.2013.03.004>.
- 597 [6] S. Lyu, L. Wang, J. Zhang, C. Liu, J. Sun, B. Peng, Y. Wang, K.G. Rappé, Y.
598 Zhang, J. Li, L. Nie, Role of Active Phase in Fischer–Tropsch Synthesis:
599 Experimental Evidence of CO Activation over Single-Phase Cobalt Catalysts,
600 *ACS Catalysis.* 8 (2018) 7787–7798. <https://doi.org/10.1021/acscatal.8b00834>.
- 601 [7] J.-X. Liu, H.-Y. Su, D.-P. Sun, B.-Y. Zhang, W.-X. Li, Crystallographic
602 Dependence of CO Activation on Cobalt Catalysts: HCP versus FCC, *Journal*
603 *of the American Chemical Society.* 135 (2013) 16284–16287.
604 <https://doi.org/10.1021/ja408521w>.
- 605 [8] N.E. Tsakoumis, J.C. Walmsley, M. Rønning, W. van Beek, E. Rytter, A.
606 Holmen, Evaluation of Reoxidation Thresholds for γ -Al₂O₃-Supported Cobalt
607 Catalysts under Fischer–Tropsch Synthesis Conditions, *Journal of the American*
608 *Chemical Society.* 139 (2017) 3706–3715.
609 <https://doi.org/10.1021/jacs.6b11872>.
- 610 [9] G.L. Bezemer, J.H. Bitter, H.P.C.E. Kuipers, H. Oosterbeek, J.E. Holewijn, X.
611 Xu, F. Kapteijn, A.J. van Dillen, K.P. de Jong, Cobalt Particle Size Effects in
612 the Fischer–Tropsch Reaction Studied with Carbon Nanofiber Supported
613 Catalysts, *Journal of the American Chemical Society.* 128 (2006) 3956–3964.
614 <https://doi.org/10.1021/ja058282w>.
- 615 [10] A. Barbier, A. Tuel, I. Arcon, A. Kodre, G.A. Martin, Characterization and
616 Catalytic Behavior of Co/SiO₂ Catalysts: Influence of Dispersion in the
617 Fischer–Tropsch Reaction, *Journal of Catalysis.* 200 (2001) 106–116.
618 <https://doi.org/10.1006/jcat.2001.3204>.

- 619 [11] A. Tuxen, S. Carenco, M. Chintapalli, C.-H. Chuang, C. Escudero, E. Pach, P.
620 Jiang, F. Borondics, B. Beberwyck, A.P. Alivisatos, G. Thornton, W.-F. Pong,
621 J. Guo, R. Perez, F. Besenbacher, M. Salmeron, Size-Dependent Dissociation
622 of Carbon Monoxide on Cobalt Nanoparticles, *Journal of the American*
623 *Chemical Society*. 135 (2013) 2273–2278. <https://doi.org/10.1021/ja3105889>.
- 624 [12] E. Rytter, N.E. Tsakoumis, A. Holmen, On the selectivity to higher
625 hydrocarbons in Co-based Fischer–Tropsch synthesis, *Catalysis Today*. 261
626 (2016) 3–16. <https://doi.org/10.1016/j.cattod.2015.09.020>.
- 627 [13] N.E. Tsakoumis, M. Rønning, Ø. Borg, E. Rytter, A. Holmen, Deactivation of
628 cobalt based Fischer–Tropsch catalysts: A review, *Catalysis Today*. 154 (2010)
629 162–182. <https://doi.org/10.1016/j.cattod.2010.02.077>.
- 630 [14] L. Vandewater, G. Bezemer, J. Bergwerff, M. Versluijshelder, B. Weckhuysen,
631 K. Dejong, Spatially resolved UV–vis microspectroscopy on the preparation of
632 alumina-supported Co Fischer–Tropsch catalysts: Linking activity to Co
633 distribution and speciation, *Journal of Catalysis*. 242 (2006) 287–298.
634 <https://doi.org/10.1016/j.jcat.2006.06.004>.
- 635 [15] J.-B. d’Espinoise de la Caillerie, M. Kermarec, O. Clause, Impregnation of
636 gamma.-Alumina with Ni (II) or Co (II) Ions at Neutral pH: Hydrotalcite-Type
637 Coprecipitate Formation and Characterization, *Journal of the American*
638 *Chemical Society*. 117 (1995) 11471–11481.
- 639 [16] J.-F. Lambert, M. Che, The molecular approach to supported catalysts
640 synthesis: state of the art and future challenges, *Journal of Molecular Catalysis*
641 *A: Chemical*. 162 (2000) 5–18. [https://doi.org/10.1016/S1381-1169\(00\)00318-](https://doi.org/10.1016/S1381-1169(00)00318-6)
642 [6](https://doi.org/10.1016/S1381-1169(00)00318-6).
- 643 [17] K. Larmier, C. Chizallet, P. Raybaud, Tuning the Metal-Support Interaction by
644 Structural Recognition of Cobalt-Based Catalyst Precursors, *Angewandte*
645 *Chemie International Edition*. 54 (2015) 6824–6827.
646 <https://doi.org/10.1002/anie.201502069>.
- 647 [18] T. Yang, M. Ehara, Probing the electronic structures of Co_n (n = 1–5) clusters
648 on γ -Al₂O₃ surfaces using first-principles calculations, *Phys. Chem. Chem.*
649 *Phys.* 19 (2017) 3679–3687. <https://doi.org/10.1039/C6CP06785A>.
- 650 [19] A.S. Andreev, M.A. Kazakova, A. V. Ishchenko, A.G. Selyutin, O.B. Lapina,
651 V.L. Kuznetsov, J.-B. d’Espinoise de Lacaillerie, Magnetic and dielectric
652 properties of carbon nanotubes with embedded cobalt nanoparticles, *Carbon*.
653 114 (2017) 39–49. <https://doi.org/10.1016/j.carbon.2016.11.070>.
- 654 [20] M.A. Kazakova, A.S. Andreev, A.G. Selyutin, A. V. Ishchenko, A. V. Shuvaev,
655 V.L. Kuznetsov, O.B. Lapina, J.-B. d’Espinoise de Lacaillerie, Co metal
656 nanoparticles deposition inside or outside multi-walled carbon nanotubes via
657 facile support pretreatment, *Applied Surface Science*. 456 (2018) 657–665.
658 <https://doi.org/10.1016/j.apsusc.2018.06.124>.
- 659 [21] I.V. Yakovlev, S.S. Yakushkin, M.A. Kazakova, S.N. Trukhan, Z.N. Volkova,
660 A.P. Gerashchenko, A.S. Andreev, A.V. Ishchenko, O.N. Martyanov, O.B.
661 Lapina, J.-B. d’Espinoise de Lacaillerie, Superparamagnetic behaviour of
662 metallic Co nanoparticles according to variable temperature magnetic

- 663 resonance, *Phys. Chem. Chem. Phys.* 23 (2021) 2723–2730.
664 <https://doi.org/10.1039/D0CP05963C>.
- 665 [22] A.S. Andreev, D.V. Krasnikov, V.I. Zaikovskii, S.V. Cherepanova, M.A.
666 Kazakova, O.B. Lapina, V.L. Kuznetsov, J. d’Espinoze de Lacaillerie, Internal
667 field ^{59}Co NMR study of cobalt-iron nanoparticles during the activation of
668 CoFe_2/CaO catalyst for carbon nanotube synthesis, *Journal of Catalysis*. 358
669 (2018) 62–70. <https://doi.org/10.1016/j.jcat.2017.11.025>.
- 670 [23] A.C. Gossard, A.M. Portis, M. Rubinstein, R.H. Lindquist, Ferromagnetic
671 Nuclear Resonance of Single-Domain Cobalt Particles, *Physical Review*. 138
672 (1965) A1415–A1421. <https://doi.org/10.1103/PhysRev.138.A1415>.
- 673 [24] V. V. Matveev, D.A. Baranov, G. Yu. Yurkov, N.G. Akatiev, I.P. Dotsenko, S.P.
674 Gubin, Cobalt nanoparticles with preferential hcp structure: A confirmation by
675 X-ray diffraction and NMR, *Chemical Physics Letters*. 422 (2006) 402–405.
676 <https://doi.org/10.1016/j.cplett.2006.02.099>.
- 677 [25] A.S. Andreev, O.B. Lapina, S.V. Cherepanova, A New Insight into Cobalt
678 Metal Powder Internal Field ^{59}Co NMR Spectra, *Applied Magnetic Resonance*.
679 45 (2014). <https://doi.org/10.1007/s00723-014-0580-0>.
- 680 [26] A.S. Andreev, J.-B. D’Espinoze De Lacaillerie, O.B. Lapina, A. Gerashenko,
681 Thermal stability and hcp-fcc allotropic transformation in supported Co metal
682 catalysts probed near operando by ferromagnetic NMR, *Physical Chemistry
683 Chemical Physics*. 17 (2015). <https://doi.org/10.1039/c4cp05327c>.
- 684 [27] Y. Liu, J. Luo, Y. Shin, S. Moldovan, O. Ersen, A. Hébraud, G. Schlatter, C.
685 Pham-Huu, C. Meny, Sampling the structure and chemical order in assemblies
686 of ferromagnetic nanoparticles by nuclear magnetic resonance, *Nature
687 Communications*. 7 (2016) 11532. <https://doi.org/10.1038/ncomms11532>.
- 688 [28] K. Pansanga, J. Panpranot, O. Mekasuwandumrong, C. Satayaprasert, J.G.
689 Goodwin, P. Praserthdam, Effect of mixed γ - and χ -crystalline phases in
690 nanocrystalline Al_2O_3 on the dispersion of cobalt on Al_2O_3 , *Catalysis
691 Communications*. 9 (2008) 207–212.
692 <https://doi.org/10.1016/j.catcom.2007.05.042>.
- 693 [29] R. Prins, On the structure of $\gamma\text{-Al}_2\text{O}_3$, *Journal of Catalysis*. 392 (2020) 336–346.
694 <https://doi.org/10.1016/j.jcat.2020.10.010>.
- 695 [30] S. V Tsybulya, G.N. Kryukova, Nanocrystalline transition aluminas:
696 Nanostructure and features of x-ray powder diffraction patterns of low-
697 temperature Al_2O_3 polymorphs, *Physical Review B*. 77 (2008) 24112.
698 <https://doi.org/10.1103/PhysRevB.77.024112>.
- 699 [31] D.F. Khabibulin, E. Papulovskiy, A.S. Andreev, A.A. Shubin, A.M. Volodin,
700 G.A. Zenkovets, D.A. Yatsenko, S.V. Tsybulya, O.B. Lapina, Surface Hydroxyl
701 OH Defects of $\eta\text{-Al}_2\text{O}_3$ and $\chi\text{-Al}_2\text{O}_3$ by Solid State NMR, XRD, and DFT
702 Calculations, *Zeitschrift Für Physikalische Chemie*. 231 (2017) 809–825.
703 <https://doi.org/10.1515/zpch-2016-0822>.
- 704 [32] L. Favaro, A. Boumaza, P. Roy, J. Lédion, G. Sattonnay, J.B. Brubach, A.M.
705 Huntz, R. Tétot, Experimental and ab initio infrared study of χ -, κ - and α -

- 706 aluminas formed from gibbsite, *Journal of Solid State Chemistry*. 183 (2010)
707 901–908. <https://doi.org/10.1016/j.jssc.2010.02.010>.
- 708 [33] S.A. Yashnik, A.V. Ishchenko, L.S. Dovlitova, Z.R. Ismagilov, The Nature of
709 Synergetic Effect of Manganese Oxide and Platinum in Pt–MnOX–Alumina
710 Oxidation Catalysts, *Top Catal.* 60 (2017) 52–72.
711 <https://doi.org/10.1007/s11244-016-0722-8>.
- 712 [34] S.A. Yashnik, V.V. Kuznetsov, Z.R. Ismagilov, Effect of χ -alumina addition on
713 H₂S oxidation properties of pure and modified γ -alumina, *Chinese Journal of*
714 *Catalysis*. 39 (2018) 258–274. [https://doi.org/10.1016/S1872-2067\(18\)63016-](https://doi.org/10.1016/S1872-2067(18)63016-5)
715 5.
- 716 [35] D.A. Nazimov, O.V. Klimov, I.G. Danilova, S.N. Trukhan, A.V. Saiko, S.V.
717 Cherepanova, Yu.A. Chesalov, O.N. Martyanov, A.S. Noskov, Effect of
718 alumina polymorph on the dehydrogenation activity of supported
719 chromia/alumina catalysts, *Journal of Catalysis*. 391 (2020) 35–47.
720 <https://doi.org/10.1016/j.jcat.2020.08.006>.
- 721 [36] K. Pansanga, J. Panpranot, O. Mekasuwandumrong, C. Satayaprasert, J.G.
722 Goodwin, P. Praserthdam, Effect of mixed γ - and χ -crystalline phases in
723 nanocrystalline Al₂O₃ on the dispersion of cobalt on Al₂O₃, *Catalysis*
724 *Communications*. 9 (2008) 207–212.
725 <https://doi.org/10.1016/j.catcom.2007.05.042>.
- 726 [37] I. V. Yakovlev, A.M. Volodin, V.O. Stoyanovskii, O.B. Lapina, A.F. Bedilo,
727 Effect of carbon coating on the thermal stability of nanocrystalline χ -Al₂O₃,
728 *Materials Chemistry and Physics*. 240 (2020) 122135.
729 <https://doi.org/10.1016/j.matchemphys.2019.122135>.
- 730 [38] I. V. Yakovlev, A.M. Volodin, V.I. Zaikovskii, V.O. Stoyanovskii, O.B.
731 Lapina, A.A. Vedyagin, Stabilizing effect of the carbon shell on phase
732 transformation of the nanocrystalline alumina particles, *Ceramics International*.
733 44 (2018) 4801–4806. <https://doi.org/10.1016/j.ceramint.2017.12.066>.
- 734 [39] P. Panissod, J.P. Jay, C. Meny, M. Wojcik, E. Jedryka, NMR analysis of buried
735 metallic interfaces, *Hyperfine Interact.* 97–98 (1996) 75–98.
736 <https://doi.org/10.1007/BF02150169>.
- 737 [40] J.R. Yates, C.J. Pickard, F. Mauri, Calculation of NMR chemical shifts for
738 extended systems using ultrasoft pseudopotentials, *Physical Review B*. 76
739 (2007) 024401. <https://doi.org/10.1103/PhysRevB.76.024401>.
- 740 [41] P.E. Blöchl, Projector augmented-wave method, *Physical Review B*. 50 (1994)
741 17953–17979. <https://doi.org/10.1103/PhysRevB.50.17953>.
- 742 [42] J.P. Perdew, J.A. Chevary, S.H. Vosko, K.A. Jackson, M.R. Pederson, D.J.
743 Singh, C. Fiolhais, Atoms, molecules, solids, and surfaces: Applications of the
744 generalized gradient approximation for exchange and correlation, *Physical*
745 *Review B*. 46 (1992) 6671–6687. <https://doi.org/10.1103/PhysRevB.46.6671>.
- 746 [43] B.G. Pfrommer, M. Côté, S.G. Louie, M.L. Cohen, Relaxation of Crystals with
747 the Quasi-Newton Method, *Journal of Computational Physics*. 131 (1997) 233–
748 240. <https://doi.org/10.1006/jcph.1996.5612>.

- 749 [44] S.J. Clark, M.D. Segall, C.J. Pickard, P.J. Hasnip, M.I.J. Probert, K. Refson,
750 M.C. Payne, First principles methods using CASTEP, *Zeitschrift Für*
751 *Kristallographie - Crystalline Materials*. 220 (2005) 567–570.
752 <https://doi.org/10.1524/zkri.220.5.567.65075>.
- 753 [45] J.P. Perdew, K. Burke, M. Ernzerhof, Generalized Gradient Approximation
754 Made Simple, *Physical Review Letters*. 77 (1996) 3865–3868.
755 <https://doi.org/10.1103/PhysRevLett.77.3865>.
- 756 [46] D. Vanderbilt, Soft self-consistent pseudopotentials in a generalized eigenvalue
757 formalism, *Physical Review B*. 41 (1990) 7892–7895.
758 <https://doi.org/10.1103/PhysRevB.41.7892>.
- 759 [47] M.F. Hansen, S. Mørup, Models for the dynamics of interacting magnetic
760 nanoparticles, *Journal of Magnetism and Magnetic Materials*. 184 (1998) L262-
761 274. [https://doi.org/10.1016/S0304-8853\(97\)01165-7](https://doi.org/10.1016/S0304-8853(97)01165-7).
- 762 [48] D.L. Leslie-Pelecky, R.D. Rieke, Magnetic Properties of Nanostructured
763 Materials, *Chem. Mater.* 8 (1996) 1770–1783.
764 <https://doi.org/10.1021/cm960077f>.
- 765 [49] O. Kitakami, H. Sato, Y. Shimada, F. Sato, M. Tanaka, Size effect on the crystal
766 phase of cobalt fine particles, *Phys. Rev. B*. 56 (1997) 13849–13854.
767 <https://doi.org/10.1103/PhysRevB.56.13849>.
- 768 [50] G. Mattei, C. de Julián Fernández, P. Mazzoldi, C. Sada, G. De, G. Battaglin,
769 C. Sangregorio, D. Gatteschi, Synthesis, Structure, and Magnetic Properties of
770 Co, Ni, and Co–Ni Alloy Nanocluster-Doped SiO₂ Films by Sol–Gel
771 Processing, *Chem. Mater.* 14 (2002) 3440–3447.
772 <https://doi.org/10.1021/cm021106r>.
- 773 [51] W. Sucksmith, The magnetic anisotropy of cobalt, *Proc. R. Soc. Lond. A*. 225
774 (1954) 362–375. <https://doi.org/10.1098/rspa.1954.0209>.
- 775 [52] C. Chizallet, C. Schlaup, E. Fonda, X. Carrier, Surface orientation dependent
776 interaction of cobalt (II) precursors with alpha-alumina, *Journal of Catalysis*.
777 394 (2021) 157–166. <https://doi.org/10.1016/j.jcat.2020.10.025>.
- 778 [53] G. Busca, The surface of transitional aluminas: A critical review, *Catalysis*
779 *Today*. 226 (2014) 2–13. <https://doi.org/10.1016/j.cattod.2013.08.003>.
- 780 [54] H. Knözinger, P. Ratnasamy, Catalytic Aluminas: Surface Models and
781 Characterization of Surface Sites, *Catalysis Reviews*. 17 (1978) 31–70.
782 <https://doi.org/10.1080/03602457808080878>.
- 783 [55] M. Digne, P. Sautet, P. Raybaud, P. Euzen, H. Toulhoat, Hydroxyl Groups on
784 γ -Alumina Surfaces: A DFT Study, *Journal of Catalysis*. 211 (2002) 1–5.
785 <https://doi.org/10.1006/jcat.2002.3741>.
- 786 [56] M. Digne, Use of DFT to achieve a rational understanding of acid-basic
787 properties of γ -alumina surfaces, *Journal of Catalysis*. 226 (2004) 54–68.
788 <https://doi.org/10.1016/j.jcat.2004.04.020>.
- 789 [57] X. Krokidis, P. Raybaud, A.-E. Gobichon, B. Rebours, P. Euzen, H. Toulhoat,
790 Theoretical Study of the Dehydration Process of Boehmite to γ -Alumina, *J.*
791 *Phys. Chem. B*. 105 (2001) 5121–5130. <https://doi.org/10.1021/jp0038310>.

- 792 [58] A.T.F. Batista, D. Wisser, T. Pigeon, D. Gajan, F. Diehl, M. Rivallan, L. Catita,
793 A.-S. Gay, A. Lesage, C. Chizallet, P. Raybaud, Beyond γ -Al₂O₃ crystallite
794 surfaces: The hidden features of edges revealed by solid-state ¹H NMR and DFT
795 calculations, *Journal of Catalysis*. 378 (2019) 140–143.
796 <https://doi.org/10.1016/j.jcat.2019.08.009>.
- 797 [59] T. Pigeon, C. Chizallet, P. Raybaud, Revisiting γ -alumina surface models
798 through the topotactic transformation of boehmite surfaces, *Journal of*
799 *Catalysis*. 405 (2022) 140–151. <https://doi.org/10.1016/j.jcat.2021.11.011>.
- 800 [60] H.C. Stumpf, A.S. Russell, J.W. Newsome, C.M. Tucker, Thermal
801 Transformations of Aluminas and Alumina Hydrates - Reaction with 44%
802 Technical Acid., *Ind. Eng. Chem.* 42 (1950) 1398–1403.
803 <https://doi.org/10.1021/ie50487a039>.
- 804 [61] V.P. Pakharukova, D.A. Yatsenko, E.Y. Gerasimov, S.V. Tsybulya, A study of
805 γ -Al₂O₃ from the viewpoint of 3D nanostructure, *Journal of Solid State*
806 *Chemistry*. 302 (2021) 122425. <https://doi.org/10.1016/j.jssc.2021.122425>.
- 807 [62] C.V. Chandran, C.E.A. Kirschhock, S. Radhakrishnan, F. Taulelle, J.A.
808 Martens, E. Breynaert, Alumina: discriminative analysis using 3D correlation
809 of solid-state NMR parameters, *Chem. Soc. Rev.* 48 (2019) 134–156.
810 <https://doi.org/10.1039/C8CS00321A>.
- 811 [63] D.A. Yatsenko, V.P. Pakharukova, S.V. Tsybulya, Low Temperature
812 Transitional Aluminas: Structure Specifics and Related X-ray Diffraction
813 Features, *Crystals*. 11 (2021) 690. <https://doi.org/10.3390/cryst11060690>.
- 814 [64] D.A. Ksenofontov, Yu.K. Kabalov, Structure refinement and thermal stability
815 of gibbsite, *Inorg Mater.* 48 (2012) 142–144.
816 <https://doi.org/10.1134/S0020168512020136>.
- 817 [65] J.M.R. Mercury, P. Pena, A.H. de Aza, D. Sheptyakov, X. Turrillas, On the
818 Decomposition of Synthetic Gibbsite Studied by Neutron
819 Thermodiffractometry, *J American Ceramic Society*. 89 (2006) 3728–3733.
820 <https://doi.org/10.1111/j.1551-2916.2006.01191.x>.
- 821 [66] T. Mitsui, T. Matsui, R. Kikuchi, K. Eguchi, Microstructural Transformation
822 with Heat-Treatment of Aluminum Hydroxide with Gibbsite Structure, *BCSJ*.
823 82 (2009) 618–623. <https://doi.org/10.1246/bcsj.82.618>.
- 824 [67] M. Salmeron, H. Bluhm, M. Tatarkhanov, G. Ketteler, T.K. Shimizu, A.
825 Mugarza, X. Deng, T. Herranz, S. Yamamoto, A. Nilsson, Water growth on
826 metals and oxides: binding, dissociation and role of hydroxyl groups, *Faraday*
827 *Discuss.* 141 (2009) 221–229. <https://doi.org/10.1039/B806516K>.
- 828 [68] X. Deng, T. Herranz, C. Weis, H. Bluhm, M. Salmeron, Adsorption of Water
829 on Cu₂O and Al₂O₃ Thin Films, *J. Phys. Chem. C*. 112 (2008) 9668–9672.
830 <https://doi.org/10.1021/jp800944r>.
- 831